Volume 16, No 1 | International Journal of Radiation Research, January 2018

A Monte Carlo study of SPECT in boron neutron capture therapy for a heterogeneous human phantom

C. Gong[1], X. Tang[1,2*], S. Fatemi[3], H. Yu[1], W. Shao[1], D. Shu[1], C. Geng[1]

[1]*Department of Nuclear Science and Engineering, Nanjing University of Aeronautics and Astronautics, Nanjing, China*
[2]*Collaborative Innovation Center of Radiation Medicine of Jiangsu Higher Education Institutions, Nanjing, China*
[3]*Department of Physics, University of Pavia, Pavia, Italy*

► ***Original article***

Corresponding authors:
Dr. Xiaobin Tang,
Fax: *+86 0255211290880407*
E-mail:
tangxiaobin@nuaa.edu.cn

Revised: March 2017
Accepted: April 2017

Int. J. Radiat. Res., January 2018; 16(1): 33-43

DOI: 10.18869/acadpub.ijrr.16.1.33

ABSTRACT

Background: Boron neutron capture therapy (BNCT) is a binary radiotherapy combining biochemical targeting with neutron irradiation. However, monitoring the boron distribution is a fundamental problem in BNCT. Prompt gamma rays emitted by boron capture reaction can be used to address the issue. ***Materials and Methods***: The general-purpose Monte Carlo toolkits Geant4 and MCNP were used for the simulations. A cubic phantom with soft tissue was used to study the prompt gamma emission during BNCT. The Chinese hybrid phantom with arbitrary tumors was constructed and used to acquire the 0.478 MeV prompt gamma rays in BNCT. Tomographic images were reconstructed with the maximum likelihood expectation maximization (MLEM) algorithm. ***Results:*** Comparison between MCNP and Geant4 showed a similar gamma rays emission rate in soft tissue. Up to 30 gamma ray peaks were found in the simulation, and 0.478 MeV prompt gamma ray from boron was clearly observed. The single brain tumor with variable diameter from 1 cm to 4 cm in the heterogeneous anthropomorphic phantom was each time found to be recognizable in the reconstructed image. Furthermore, in a patient with four tumors, the variable distance between the source and the tumors leads to a neutron attenuation thus resulting in an inhomogeneous number of prompt gammas. ***Conclusion:*** The SPECT system for a heterogeneous phantom in BNCT was simulated with Geant4. The results show that BNCT-SPECT is valid for the reconstruction of the boron capture interaction position for a heterogeneous patient.

Keywords: *Boron neutron capture therapy; single photon emission computed tomography; prompt gamma; Geant4; MLEM.*

INTRODUCTION

Cancer remains a major cause of death for humans nowadays, one of the main methods for cancer therapy is radiation therapy, whose principle is to kill the tumor by delivering the highest dose to the tumor region while minimizing the radiation damage to normal tissue. Boron neutron capture therapy (BNCT) [1-5] is a binary radiotherapy combining biochemical targeting with neutron irradiation. The concept of BNCT is to use the nuclear capture reaction that occurs when non-radioactive ^{10}B is irradiated with thermal neutrons yielding excited ^{11}B, which then decays into α particles and ^{7}Li nuclei. The high linear energy transfer of α and ^{7}Li can be used to induce the death of tumor cells. At the same time, prompt gamma rays are emitted during de-excitation of excited ^{7}Li to the ground state at the reaction point.

One of the crucial problems to be considered in BNCT applications is to determine the boron distribution in real time. The 0.478 MeV prompt gamma rays might be used to address the issue since they are emitted *in-situ* during the neutron capture interaction. Verbakel *et al.* first developed a γ-ray telescope system to detect the 0.478 MeV prompt gamma rays [6-8]. Kobayashi *et al.* first proposed the concept of PG-SPECT, in

[Downloaded from ijrr.com on 2026-11-29]

[DOI: 10.18869/acadpub.ijrr.16.1.33]

which single-photon emission computed tomography (SPECT) was combined with prompt γ-ray analysis, for providing noninvasive three-dimensional dose estimation during clinical BNCT irradiations [9]. Rosenschöld *et al.* reported the feasibility of a prototype of a pin-hole collimator with a HPGe crystal detector system mounted on a C-bow device for prompt gamma tomography during BNCT both with a ^{137}Cs-source and a ^{131}I-phantom [10]. Minsky *et al.* developed a SPECT system for obtaining boron dose maps during a BNCT irradiation in water phantom [11-14]. Furthermore, Murata *et al.* studied the feasibility of CdTe detector in BNCT-SPECT [15,16], and Katabuchi *et al.* reported the feasibility of the pinhole camera system for online dosimetry in BNCT [17]. In addition, feasibility studies of the SPECT application in BNCT treatments were conducted to compute online boron dose maps from the perspective of simulation [18]. Yoon DK *et al.* studied the prompt gamma ray image through the simple spherical water phantom simulation with MCNPX and performed the fast reconstruction of a prompt gamma ray image with the graphics processing unit computation [19-21].

However, the effects of SPECT in BNCT have not yet been studied in a real human heterogeneous patient. In this study, a simulation was conducted to study the effects of BNCT-SPECT in a brain tumor phantom with Monte Carlo codes. First, a cubic geometry with soft tissue was used to study the potential background in BNCT-SPECT, and to cross-check the two Monte Carlo codes, MCNP and Geant4. Then, an anthropomorphic phantom with different brain tumors was constructed for the Monte Carlo simulations. The BNCT-SPECT in the heterogeneous phantom was simulated, and the tomography images were reconstructed with the maximum likelihood expectation maximization (MLEM) algorithm.

MATERIALS AND METHODS

This study was performed using the Monte Carlo simulation toolkit Geant4 [22], which is a general-purpose radiation transportation toolkit, widely used in the field of medical physics [23,24]. The simulated BNCT-SPECT system in this study was composed of the neutron source, the Chinese Male phantom with brain tumors, the SPECT detectors and collimators. In the Chinese Male phantom, the main boron uptake regions (BURs) were in brain tumors. An epithermal neutron beam, as shown in Figure 1 irradiated the patient head. With the rotation of the detectors, the prompt gamma generated from the interaction of neutron and ^{10}B was tallied for each angle.

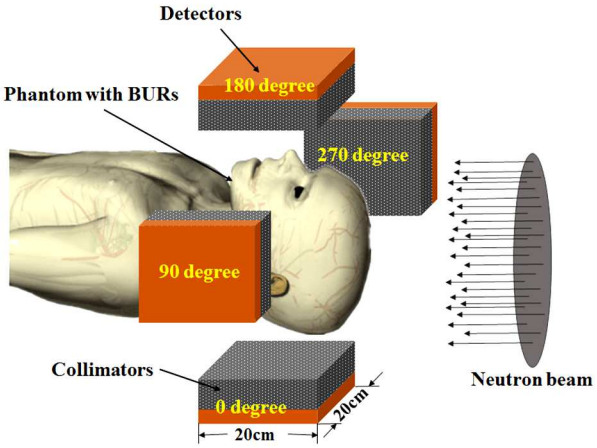

Figure 1. Diagram of BNCT-SPECT system in the Monte Carlo simulation (the labeled angles represent the position of the rotated detector).

Neutron source

An epithermal neutron flux of 1×10^9 neutron $cm^{-2} \bullet s^{-1}$ is often required to prevent the increase of the undesired dose in normal tissues surrounding the tumors in BNCT. The epithermal neutron beam from Massachusetts Institute of Technology (MIT) research reactor was used as the neutron source to irradiate the phantom in this study. The beam has an epithermal fluence rate of about 3.71×10^9 neutron $cm^{-2} \bullet s^{-1}$, and the detailed neutron spectrum of MIT reactor with 10-mm lithium filter can be found in the reference [25]. The lithium filter could decrease the thermal neutrons, and therefore increase the average energy of the epithermal neutron and the dose delivered to the tumor while decreasing the radiation dose absorbed in healthy tissues. The circular source had 20 cm diameter, which completely encompassed the tumor volume. In

[Downloaded from ijrr.com on 2026-11-29]

[DOI: 10.18869/acadpub.ijrr.16.1.33]

addition, the distance between the neutron source and the head phantom was set as 20 cm.

Construction of brain tumors in Chinese hybrid male phantom

The Chinese hybrid male phantom [26,27], which was established based on the mesh modeling method with great flexibility and reality, was utilized in this study. The model can be adjusted with various characteristics such as gender, age, weight, height, and volumes of organs. The construction procedure for the phantom geometry and materials can be found in detail in a previous publication [26]. Tissue or organ compositions were taken from the data in ICRU-46 [28] and ICRP-89 [29]. Based on the established Chinese hybrid male phantom, the tumors were constructed into the head of the phantom with Rhinoceros, a commercial 3D computer graphics and computer-aided design application software. Two kinds of scenarios, i.e. one and four tumors in a patient, were considered in this study. For the first case, we constructed tumors with four different diameters (4 cm, 3 cm, 2 cm, and 1 cm) at the same center point. For the second case, we constructed four tumors with different diameters symmetrically in the same phantom. Figure 2 shows the established Chinese hybrid male phantom and the cross-section images for the second case. While figure 2(a) shows the frontal view of Chinese hybrid male phantom, figure 2(b) and figure 2(c) show the internal organs of Chinese hybrid male phantom. The detailed setup of tumors can be seen in figure 2 (c), and their density was set as 2.08 g/cm^3 [19,20]. To reduce the computational time, only the head of the Chinese hybrid male phantom, i.e. without the lower part of human body, was considered in this study. This head phantom used in this study included various structures like skin, brain, ears, eyes, skull, teeth, thyroid, tongue, mandible, sialaden, ET, vessels, lymphonode, muscle and tonsil.

To simulate as a voxelized geometry in Geant4, each organ was exported and then voxelized with Binvox [30], which used a ray-stabbing method to voxelize 3D models. Finally, an *in-house* code was developed to integrate each organ into the final whole voxelized phantom, in which every organ had an index representing it. Figures 2(d-f) show the transverse plane, the coronal plane, and the sagittal plane of the final head phantom.

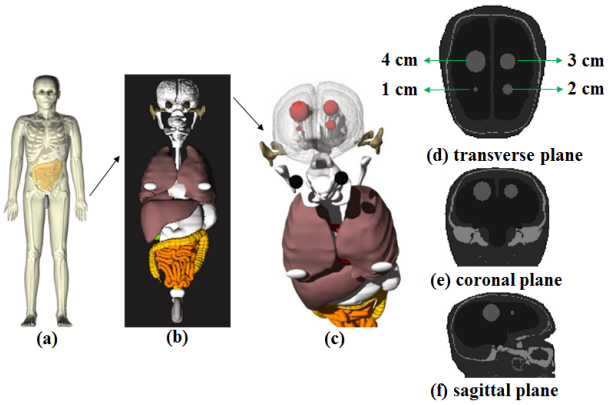

Figure 2. The construction of tumors with four different diameters (1 cm, 2 cm, 3 cm, and 4 cm) in the Chinese hybrid male phantom, and the three views of head phantom with four tumors were presented.

Detectors configuration

Four sets of detectors were simulated to detect the 0.478 MeV prompt gamma rays emitted from the thermal neutron capture reaction on boron in the BURs for each simulation. The purpose of this setting was to reduce the computational time. A set of detectors is composed of 200 × 200 array, i.e. there are 40000 sub-detectors (i.e. Y(1) to Y (40000) in Figure 3) in one set of the detector. The columns and rows in Figure 3 represent the detectors, and the column index and row index represent the detector index number. The direction of 0 degree was defined as the original setting of detectors direction as shown in figure 1. Detectors were then clockwise rotated. The collimator was simulated through a direction selection criterion which means that the particle direction should be almost perpendicular (±1 degree) to the detector.

Image reconstruction algorithm

The detectors were rotated around the patient from 0 to 80 degrees (rotation step of 10°), i.e. a total of 36 angles (from 0° to 350°) were calculated around the patient with four angles in one simulation, as shown in figure 1.

[Downloaded from ijrr.com on 2026-11-29]

[DOI: 10.18869/acadpub.ijrr.16.1.33]

The iterative reconstruction method, MLEM algorithm [31], was used to obtain the tomographic images in this study. The principle of the iterative algorithms is to obtain a solution by successive estimates. The projections corresponding to the current estimate are compared with the measured projections. The comparison result was used to modify the current estimate, thereby creating a new estimate. The modification criterion of each iteration in MLEM is the maximization of the likelihood of the reconstructed image. The general formula of the method in this study is,

$$\text{Image}^{(k+1)} = \text{Image}^{(k)} \times \text{Normalized Backprojection of} \left(\frac{\text{Measured projections}}{\text{Projections of image}^{(k)}} \right) \quad (1)$$

where k is the iteration number. The starting image (k=0) is the image obtained by the Back-Projection method [31]. The total reconstructed images were composed of 200 layers, and each layer was 1 mm thick. The layer indexes of 1 and 200 indicated the bottom and the top of the head, respectively.

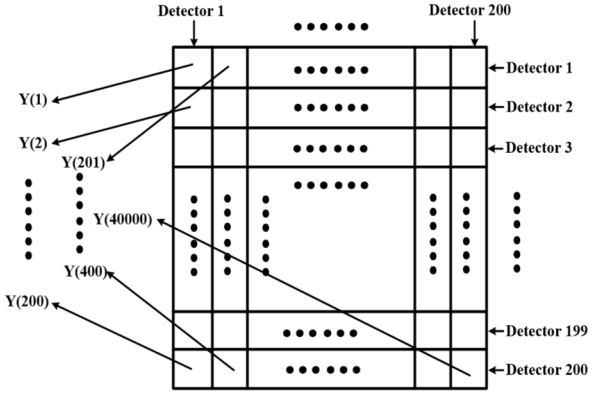

Figure 3. Arrangement of the detectors.

RESULTS

Prompt gamma ray emission during BNCT

A phantom with cubic geometry (14 × 14 × 10 cm^3) was used and a 1 eV neutron point source was emitted 0.5 cm away from phantom surface. The boron concentration in the scored volume was 50 ppm [32]. The ICRU recommended soft tissue composition [28] was used in this study. The simulation was performed both in MCNP and Geant4 in order to check the physical setting in Geant4, and the statistical errors were lower than 5%. Tally 4 was used in the MCNP. The thermal scattering effect was considered both in MCNP and Geant4 simulations, as recommended in the previous work [33]. The prompt gamma fluences were recorded at various depths, i.e. 0 cm, 3 cm, 5 cm, 7 cm, and 10 cm. Results were normalized with the initial particle number. Figure 4 shows the prompt gamma fluence spectrum per primary neutron obtained by MCNP and Geant4 at the depth of 0 cm. The blue line is the spectrum of the prompt gamma ray from the phantom by MCNP, and the red dots are the spectrum obtained by Geant4. Table 1 shows the possible gamma ray energies and cross sections generated with elements of soft tissue, which are taken from the PGAA Prompt Gamma Database [34]. The black dots in figure 4 are the markers for the peaks, whose information are taken from the table 1. Figure 5 shows the prompt gamma fluence generated at different depths of the cubic phantom. The width of energy bin is 2 keV in figures 4 and 5.

Tomographic images for the same tumor with different volumes

In this section, one brain tumor with different diameters of 1 cm, 2 cm, 3 cm, and 4 cm located in the same position was simulated. Figure 6 shows the projection images of the same detector (0 degree) for the four simulations, and the values in the Figure 6 stand for the counts of 0.478 MeV prompt gamma ray in the detector. Figures 7-10 show the reconstructed tomographic images of the tumors with different diameters of 1 cm, 2 cm, 3 cm, and 4 cm, respectively. Here, the values in these figures are relative value, which stand for the normalized value with the initial particle number. Figures 7 (a), 8(a), 9(a) and 10(a) show the entrance directions of the neutron beam and Figures 7(b), 8(b), 9(b) and 10(b) show five successive layers of reconstructed tomographic images in a transverse plane. Figures 7(c), 8(c), 9(c) and 10 (c) show the simulated sinograms of the tumors with different volumes.

[Downloaded from ijrr.com on 2026-11-29]

[DOI: 10.18869/acadpub.ijrr.16.1.33]

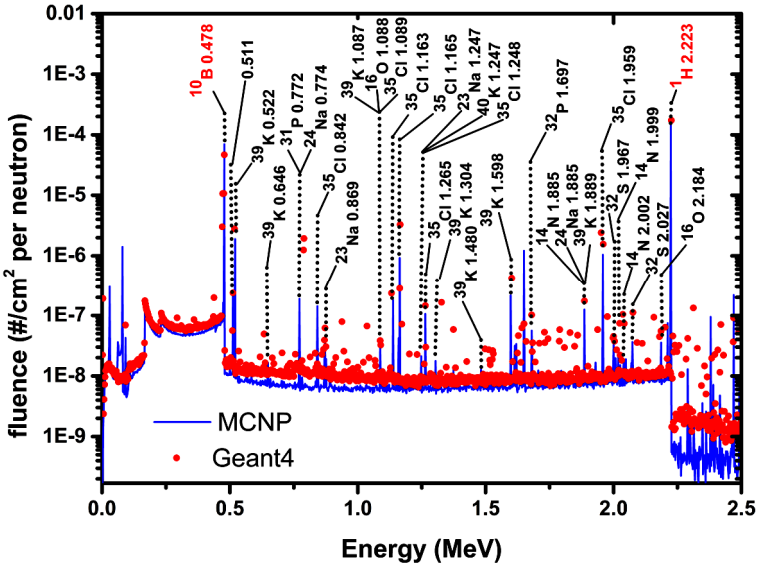

Figure 4. Prompt gamma fluence spectrum per primary neutron by MCNP and Geant4 calculation.

Table 1. Energy-ordered table of the most intense thermal neutron capture gamma rays (Eγ < 2.5 MeV)

	E_γ (MeV)	σ_γ (barns)	E_γ (σ_γ) for intense gamma rays
^{1}H	2.223	3.326E-01	2.223(3.326E-01)
^{10}B	0.478	3837	0.478(716)
^{12}C	1.262	1.24E-03	0.595(9.50E-06), 1.857(6.20E-06)
^{14}N	1.885	1.47E-02	0.584(4.29E-04), 0.908(1.27E-04), 1.012(1.08E-04), 1.678 (6.30E-03), 1.681 (1.29E-03), 1.784(1.95E-04), 1.854(5.08E-04), 1.999(3.23E-03), 2.002(1.90E-04), 2.031 (5.80E-05), 2.247(1.20E-05), 2.262(6.10E-05), 2.293 (3.60E-05)
^{16}O	1.088	1.58E-04	0.871(1.77E-04), 2.184(1.64E-04)
^{23}Na	0.869	1.08E-01	0.091(2.35E-01), 0.774(3.84E-04), 0.874(7.60E-02), 1.247 (1.22E-03), 1.636 (2.50E-02), 1.885(3.90E-03), 2.025 (3.41E-02), 2.208(2.59E-02), 2.414(2.37E-02)
^{31}P	0.512	7.90E-02	0.078(5.90E-02), 0.637(3.11E-02), 0.772(4.30E-04), 1.071 (2.49E-02), 1.613 (4.60E-04), 2.114(1.15E-02)
^{32}S	0.841	3.47E-01	1.697(1.25E-02), 1.967(3.57E-03), 2.027(6.00E-5), 2.379 (2.08E-01)
^{35}Cl	1.165	8.91	0.478(2.70E-02), 0.517(7.58), 0.786(3.42), 0.788(5.42), 0.842(1.20E-02), 1.089(0.01), 1.163(0.76), 1.248(0.02), 1.265(2.10E-02), 1.601(1.21), 1.951(6.33), 1.959(4.1)
^{39}K	1.159	0.16	0.522(3.47E-02), 0.646(4.51E-02), 0.770(9.03E-01), 1.087 (2.22E-02), 1.247 (7.84E-02), 1.304(5.50E-02), 1.480 (3.53E-02), 1.598(5.60E-03), 1.889(1.50E-03), 1.930(0.01)

[Downloaded from ijrr.com on 2026-11-29]

[DOI: 10.18869/acadpub.ijrr.16.1.33]

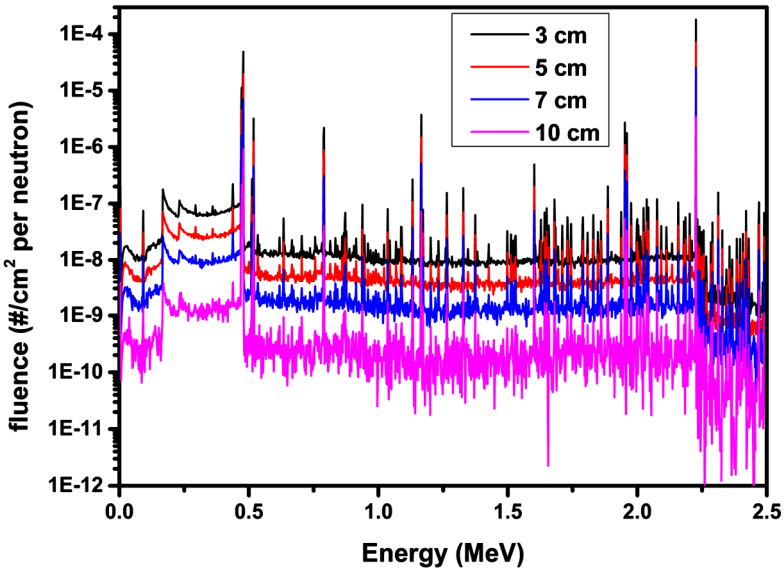

Figure 5. Prompt gamma fluence spectrum per primary neutron by Geant4 at different depths of the cubic phantom.

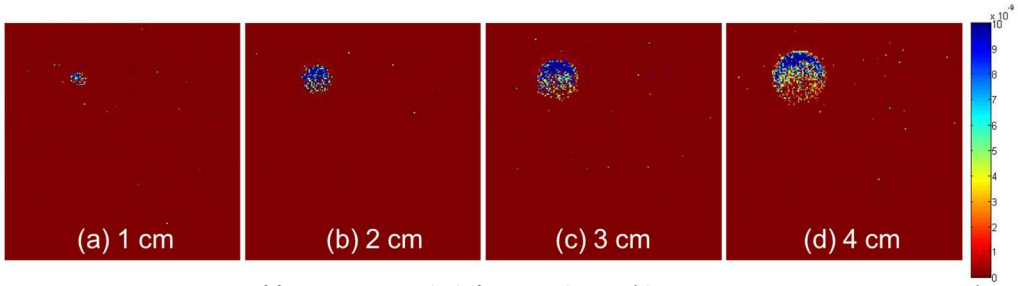

Figure 6. Projection images of four tumors with different volumes (diameter = 1 cm, 2 cm, 3 cm, 4 cm).

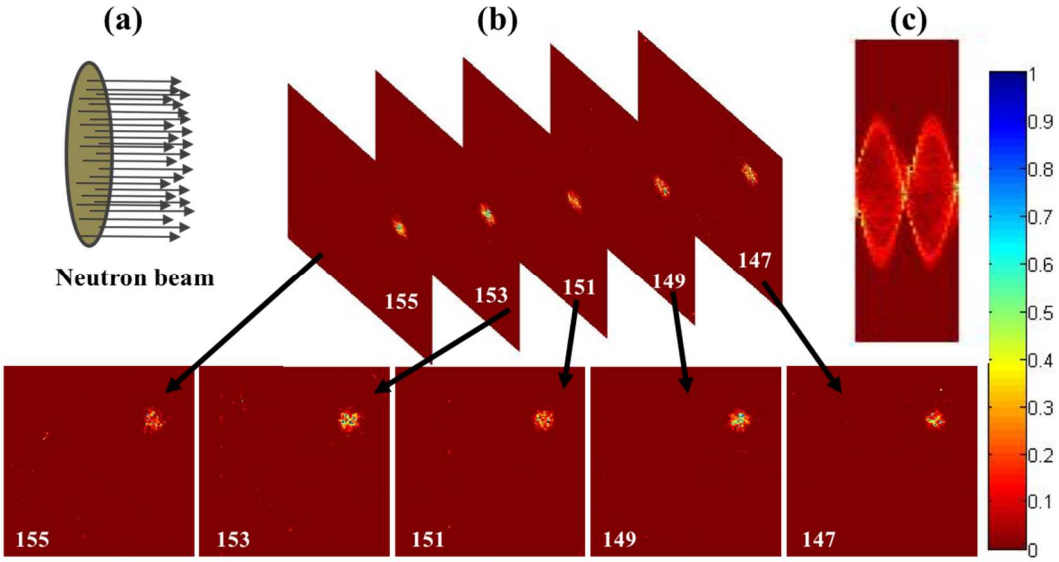

Figure 7. Reconstructed tomographic images of 1 cm diameter tumor by 4 iterations (the number in the figure indicates the layer number). (**a**) illustration of the neutron beam direction; (**b**) reconstructed image; (**c**) simulated sinogram.

[Downloaded from ijrr.com on 2026-11-29]

[DOI: 10.18869/acadpub.ijrr.16.1.33]

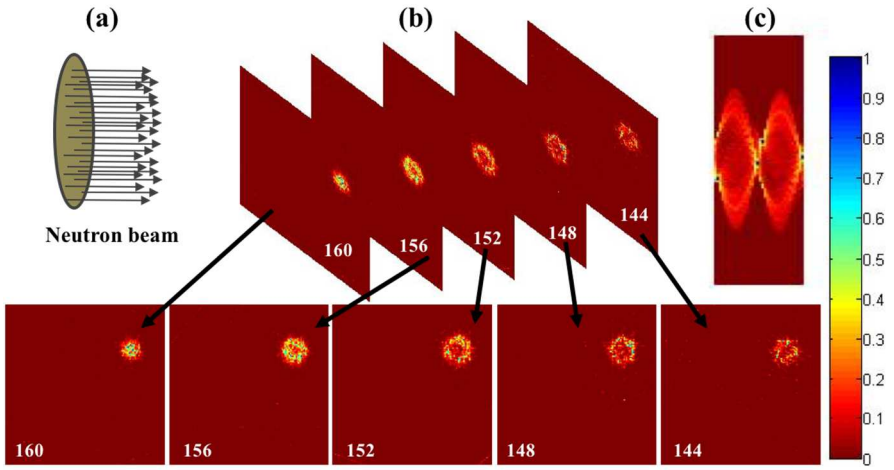

Figure 8. Reconstructed tomographic images of 2 cm diameter tumor by 4 iterations (the number in the figure indicates the layer number). (**a**) illustration of the neutron beam direction; (**b**) reconstructed image; (**c**) simulated sinogram.

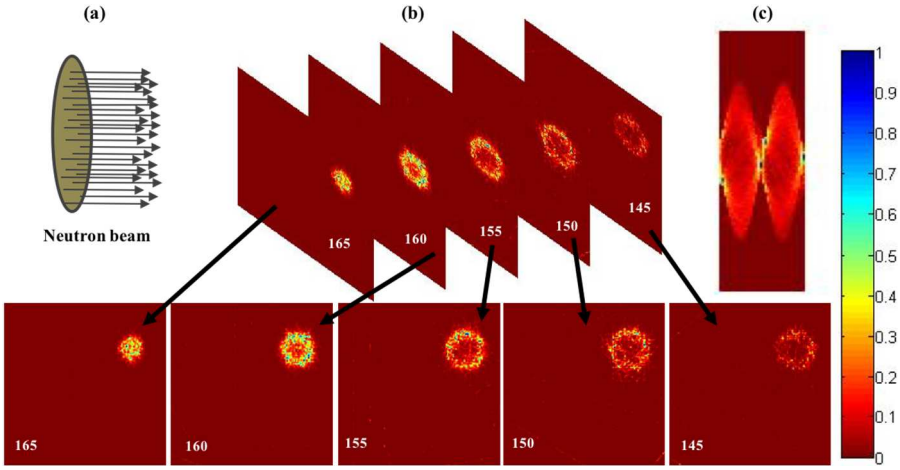

Figure 9. Reconstructed tomographic images of 3 cm diameter tumor by 4 iterations (the number in the figure indicates the layer number). (**a**) illustration of the neutron beam direction; (**b**) reconstructed image; (**c**) simulated sinogram.

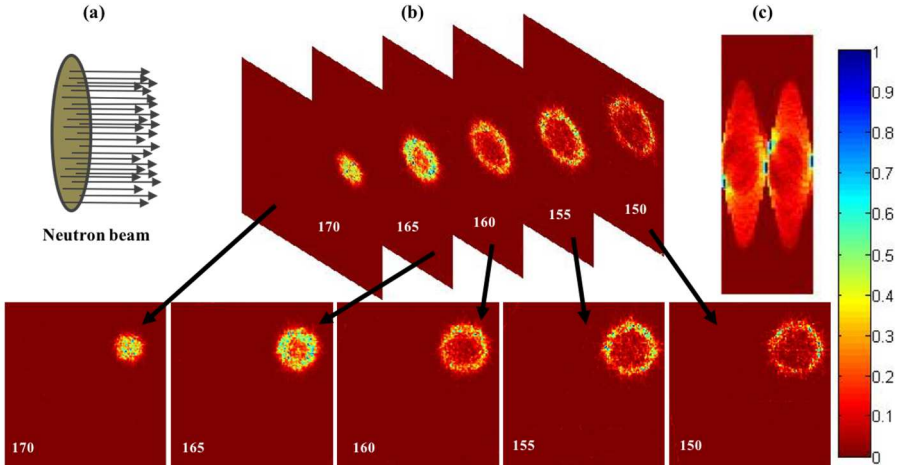

Figure 10. Reconstructed tomographic images of 4 cm diameter tumor by 4 iterations (the number in the figure indicates the layer number): (**a**) illustration of the neutron beam direction; (**b**) reconstructed image; (**c**) simulated sinogram.

[Downloaded from ijrr.com on 2026-11-29]

[DOI: 10.18869/acadpub.ijrr.16.1.33]

Tomographic images with four tumor volumes

Figure 11 shows eight projection images selected among 36 projection directions for the simulation of the case of four different tumors in the same phantom, and the values in it stand for the counts of 0.478 MeV prompt gamma ray in the detector. Due to the overlap of the projections, three high signal regions can be observed in figures 11(b), 11(e), 11(f), and 11 (g), which represent the 4 projection directions of 50°, 200°, 250°, and 300°, respectively. For the projection image in the direction of 150°, four high signal regions were observed in figure 11(d). Figure 12 shows the reconstructed tomographic images of different layers for the case of four tumors in the same phantom, and the values in it stand for the normalized value with the initial particle number. Figure 12(a) indicates the entrance direction of the neutron beam, and figure 12(b) shows five successive layers of reconstructed images with all the projections of 36 different directions. Figure 12 (c) shows the simulated sinogram.

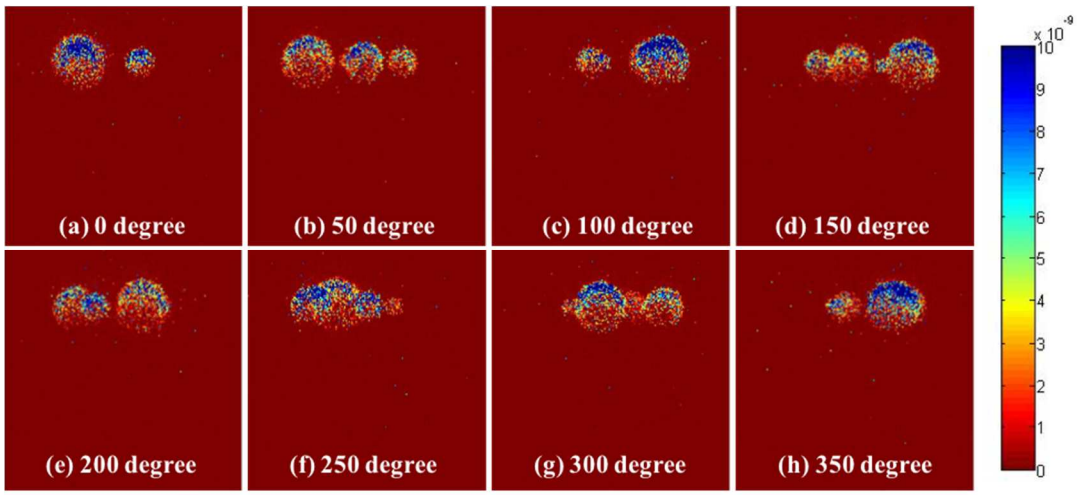

Figure 11. Projection images for the case with four difference tumors.

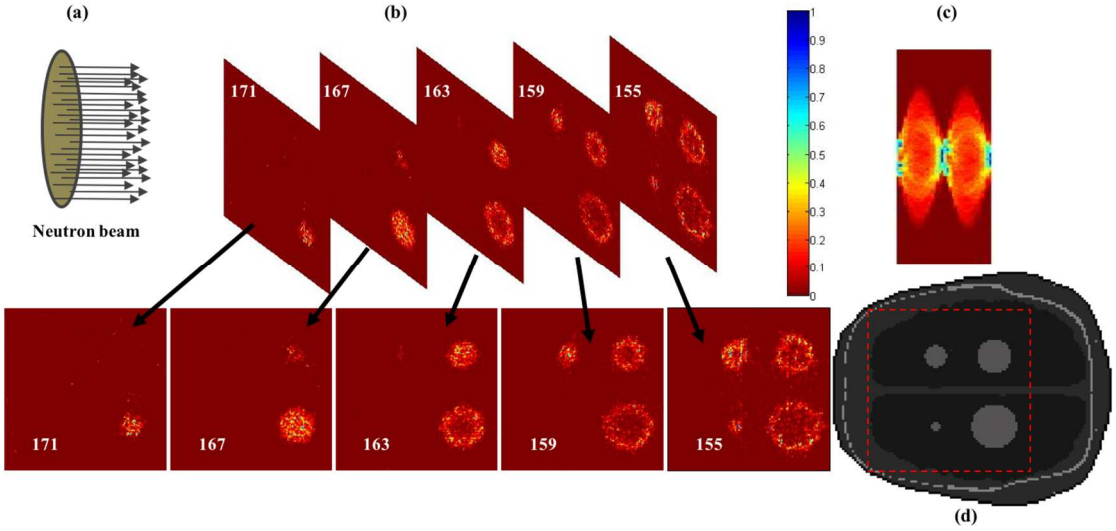

Figure 12. Reconstructed tomographic images with four tumor volumes with 7 iterations (the number in the figure indicates the layer number). (**a**) illustration of the neutron beam direction; (**b**) reconstructed image; (**c**) simulated sinogram; (d) original phantom.

[Downloaded from ijrr.com on 2026-11-29]

[DOI: 10.18869/acadpub.ijrr.16.1.33]

DISCUSSION

Although water has been widely used as a surrogate material of human tissues for dose calculations in photon and proton therapy, it is not suitable for neutron therapies because of the strong element dependence and energy dependence of neutron interaction cross sections. The neutron capture reaction with elements of human tissue would potentially generate gamma rays with different characteristic energies, thus forming the undesired background for BNCT-SPECT of 0.478 MeV gamma rays. In this study, the prompt gamma rays emitted by the nuclear reactions in human soft tissue during BNCT were analyzed. As shown in figure 4, the prompt gamma fluence spectrum generated in the human soft tissue per primary neutron indicates good agreement between the results calculated with Geant4 and those obtained by MCNP, which validates our Geant4 simulation.

As labeled in figure 4 according to Table 1, up to 30 gamma ray peaks were found in the simulation results. Of special interest would be the energy bins containing the two strongest lines, 0.478 and 2.223 MeV, the de-excitation gamma rays from $^{10}B(n,a)^{7}Li$ and $^{1}H(n, \gamma)^{2}H$, respectively. The peak value (2.223 MeV) of the fluence emitted from the neutron hydrogen capture indicates the highest prompt gamma ray yield, which is due to its highest concentration in organic bodies and the high cross-section of hydrogen. The 2.223 MeV gamma rays are the highest background for BNCT-SPECT of 0.478 MeV gamma rays, this information can also be measured to provide useful information about neutron distribution inside the phantom. The intensity of the 0.478 MeV gamma ray is comparable to that of the 2.223 MeV gamma ray, even though there is a relatively lower mass fraction of ^{10}B in the phantom. Comparing the prompt gamma fluence spectrum obtained by Geant4 for various depths in the phantom, we found that that the fluence of prompt gamma decreases with increased depth due to the attenuation of neutrons and to the inverse-square law, as shown in figure 5.

While the previous simulation studies were mostly focused on the principle of BNCT-SPECT with very simple geometry settings [19,20], in this study, we go one step further to realize the prompt gamma tomography for brain tumor cases in a heterogeneous phantom, and the reconstruction of the images was obtained from 36 projections with the MLEM algorithm. First, a single tumor inside the brain was studied. The reconstructed tomographic images after four iterations can be seen in figures 7-10. The tumor volume can be clearly observed in the proximal regions, i.e. close to the neutron source, from the reconstructed images. For the case with four tumor volumes in the same phantom, the reconstructed tomographic images after seven iterations can be seen in figure 12. For both one and four tumor cases, the BURs can be well recognized in the reconstructed tomographic images with high resolution. As shown in figure 12, the four circular areas well agree with the position of the BUR region in the patient (figure 12(d)). When comparing the tomographic images in this study to the results in other papers [14,19,20], the image quality has a better resolution than that of simple geometric models. As shown in figures 7(b)-10(b) and figure 12(b), the intensity of prompt gamma rays in tumor is decreasing as the radial distance from the source decreases, especially inside the tumor area. Moreover, the intensity of prompt gamma rays in tumor decreases with the depth of the tumor as shown in figure 5. The reason for this effect is that with increased distance from the neutron source, the neutron fluence is reduced by the upstream reactions and also the inverse-square law. Considering the neutron attenuation could result in low dose for the innermost regions of the tumor, to achieve a better tumor coverage multiple-field irradiation can be used to improve the tumor dose distribution, as suggested in Fujimoto *et al.* [35] as well.

CONCLUSION

Currently, the ability to accurately monitor boron distribution in the patient remains pivotal in the clinical application of BNCT. Using the 0.478 MeV prompt gamma ray to reconstruct the

[Downloaded from ijrr.com on 2026-11-29]

[DOI: 10.18869/acadpub.ijrr.16.1.33]

spatial distribution of boron was expected to pave the way to better understand the issue and provide the clinical confidence for treatment. In this study, the Monte Carlo simulation investigated the gamma rays emitted from the thermal capture interaction in the soft tissue. In this study the conceptual model of the BNCT-SPECT was validated in a heterogeneous human phantom and its first BNCT-SPECT image was reconstructed with the MLEM reconstruction algorithm. The influence of tumor size on boron distribution and image quality were discussed. In the future study, we aim to improve the radiation detector and the collimator system, and we would like to focus on designing a BNCT-SPECT system to handle the complicated neutron and gamma ray background from human tissues based on the considerations of more realistic treatment situations.

ACKNOWLEDGEMENTS

This work was financially supported by the Priority Academic Program Development of Jiangsu Higher Education Institutions, the National Natural Science Foundation of China [grant number 11475087], the National Key Research and Development Program (Grant No. 2016YFE0103600 and 2017YFC0107700), and the Funding of Jiangsu Innovation Program for Graduate Education [grant number KYLX15_0303].

Conflicts of interest*: *Declared none.

REFERENCES

1. Sauerwein WAG (2012) Principles and Roots of Neutron Capture Therapy. In: Neutron Capture Therapy, (Sauerwein WAG, Wittig A, Moss R, Nakagawa Y, eds.), Springer-verlag: *Berlin Heidelberg, Heidelberg. p. 1–16*.
2. Lee PY, Liu YH, Jiang SH (2014) Dosimetric performance evaluation regarding proton beam incident angles of a lithium-based AB-BNCT design. *Radiat Prot Dosim,* ***161(1-4):*** *403–9*.
3. Fantidis JG, Saitioti E, Bandekas DV, Vordos N (2013) Optimised BNCT facility based on a compact D-D neutron generator. *Int J Radiat Res,* ***11(4):*** *207–214*.
4. Yu HY, Tang XB, Shu DY, Geng CR, Gong CH, Hang S, *et al.* (2017) Impacts of multiple-field irradiation and boron concentration on the treatment of boron neutron capture therapy for non-small cell lung cancer. *Int J Radiat Res,* ***15 (1):*** *1-13*.
5. Abtahi SM, Aghamiri SMR, Khalafi H, Rahmani F (2014) An investigation into the potential applicability of gel dosimeters for dosimetry in boron neutron capture therapy. *Int J Radiat Res,* ***12(2):*** *139–149*.
6. Verbakel WFAR and Stecher-Rasmussen F (2001) On-line reconstruction of low boron concentrations by in vivoγ-ray spectroscopy for BNCT. *Phys Med Biol,* ***46(3):*** *687–701*.
7. Verbakel WFAR, Sauerwein W, Hideghety K (2003) Boron concentrations in brain during boron neutron capture therapy: in vivo measurements from the phase I trial EORTC 11961 using a gamma-ray telescope. *Int J Radiat Oncol Biol Phys,* ***55(3):****743-756*.
8. Verbakel WFAR and Stecher-Rasmussen F (1997) A γ-ray telescope for on-line measurements of low boron concentrations in a head phantom for BNCT. *Nucl Instrum Methods Phys Res Sect A,* ***394(1-2):*** *163–72*.
9. Kobayashi T, Sakurai Y, Ishikawa M (2000) A noninvasive dose estimation system for clinical BNCT based on PG-SPECT—Conceptual study and fundamental experiments using HPGe and CdTe semiconductor detectors. *Med Phys,* ***27(9):*** *2124–32*.
10. Rosenschöld PMA, Minarik D, Östlund C, Ljungberg M, Ceberg C (2006) Prompt gamma tomography during BNCT—a feasibility study. *J Instrum,* ***1(05):*** http://dx.doi.org/10.1088/1748-0221/1/05/P05003
11. Minsky DM, Valda AA, Kreiner AJ, Green S, Wojnecki C, Ghani Z (2011) First tomographic image of neutron capture rate in a BNCT facility. *Appl Radiat Isot,* ***69(12):*** *1858–61*.
12. Minsky DM, Valda A, Kreiner AJ, Burlon AA, Green S, Wojnecki C, *et al.* (2010) Progress In The Development Of A Tomographic SPECT System For Online Dosimetry In BNCT. *AIP Conference Proceedings,* ***1265:*** *415–418*.
13. Minsky DM, Valda AA, Kreiner AJ, Green S, Wojnecki C, Ghani Z (2009) Experimental feasibility studies on a SPECT tomograph for BNCT dosimetry. *Appl Radiat Isot,* ***67(7-8):*** *S179–82*.
14. Valda A, Minsky DM, Kreiner AJ, Burlon AA, Somacal H (2005) Development of a tomographic system for online dose measurements in BNCT (Boron Neutron Capture Therapy). *Braz J Phys,* ***35(3B):*** *785–788*.
15. Murata I, Mukai T, Ito M, Miyamaru H, Yoshida S (2011) Feasibility study on BNCT-SPECT using a CdTe detector. *Prog Nucl Sci Technol,* ***1:*** *267-270*.
16. Manabe M, Nakamura S, MURATA I (2016) Study on measuring device arrangement of array-type CdTe detector for BNCT-SPECT. *Rep Radiother Oncol,* ***21(2):*** *102–107*.
17. Katabuchi T, Hales B, Hayashizaki N, Igashira M, Khan Z, Kobayashi T, *et al.* (2014) Feasibility study on pinhole camera system for online dosimetry in boron neutron capture therapy. *Appl Radiat Isot,* ***88:*** *139–142*.
18. Wittig A and Sauerwein WAG (2012) Boron analysis and boron imaging in BNCT. In: Neutron Capture Therapy,

[Downloaded from ijrr.com on 2026-11-29]

[DOI: 10.18869/acadpub.ijrr.16.1.33]

(Sauerwein WAG, Wittig A, Moss R, Nakagawa Y, eds.), Springer-verlag: Berlin Heidelberg, Heidelberg. p. 163–188.
19. Yoon D-K, Jung J-Y, Hong KJ, Lee KS, Suh TS (2015) GPU-based prompt gamma ray imaging from boron neutron capture therapy. *Med Phys,* ***42(1):*** *165–169*.
20. Yoon D-K, Jung J-Y, Jo Hong K, Suk Suh T (2014) Tomographic image of prompt gamma ray from boron neutron capture therapy: A Monte Carlo simulation study. *Appl Phys Lett,* ***104(8):*** *083521*.
21. Jung J-Y, Lu B, Yoon D-K, Hong KJ, Jang H, Liu C, *et al*. (2016) Therapy region monitoring based on PET using 478 keV single prompt gamma ray during BNCT: A Monte Carlo simulation study. *Phys Medica,* ***32(4):*** *562–567*.
22. Geant4 Collaboration (2002) Geant4 - A Simulation Toolkit. *Nucl Instrum Meth A,* ***506(3):*** *250-303*.
23. Guan F, Bronk L, Titt U, Lin SH, Mirkovic D, Kerr MD, *et al.* (2015) Spatial mapping of the biologic effectiveness of scanned particle beams: towards biologically optimized particle therapy. *Sci Rep,* ***5:*** *9850*.
24. Guan F, Peeler C, Bronk L, Geng C, Taleei R, Randeniya S, *et al.* (2015) Analysis of the track- and dose-averaged LET and LET spectra in proton therapy using the geant4 Monte Carlo code. *Med Phys,* ***42(11):*** *6234–47*.
25. Mirzaei D, Miri-Hakimabad H, Rafat-Motavalli L (2014) Depth dose evaluation for prostate cancer treatment using boron neutron capture therapy. *J Radioanal Nucl Ch,* ***302 (3):*** *1095–1101*.
26. Geng C, Tang X, Hou X, Shu D, Da Chen (2014) Development of Chinese hybrid radiation adult phantoms and their application to external dosimetry. *Sci China Technol Sci,* ***57 (4):*** *713–719.*
27. Geng C, Tang X, Qian W, Guan F, Johns J (2015) Calculations of S values and effective dose for the radioiodine carrier and surrounding individuals based on Chinese hybrid reference phantoms using the Monte Carlo technique. *J Radiol Prot,* ***35:*** *707–717*.
28. ICRU Report 46 (1992) Photon, Electron, Proton and Neutron Interaction Data for Body Tissues. ICRU, Bethesda, MD.
29. ICRP Publication 89 (2002) Basic anatomical and physiological data for use in radiological protection reference values. *Ann ICRP,* ***32(3-4):*** *1–277*.
30. Binvox [Internet]. [cited 2016 Feb 26]. Available from: http://www.patrickmin.com/binvox/.
31. Bruyant PP (2002) Analytic and Iterative Reconstruction Algorithms in SPECT. *J Nucl Med,* ***43(10):****1343–58.*
32. Chin MPW, Spyrou NM (2009) Monitoring of gamma emission and neutron transmission during boron neutron capture treatment delivery. *J Radioanal Nucl Ch,* ***281(1):*** *149–52*.
33. Geng C, Tang X, Guan F, Johns J, Vasudevan L, Gong C, *et al.* (2016) GEANT4 calculations of neutron dose in radiation protection using a homogeneous phantom and a Chinese hybrid male phantom. *Radiat Prot Dosim,* ***168(4):*** *433–40*.
34. PGAA Database Files [Internet]. International Atomic Energy Agency. 1999–2003 [cited 2016 Feb 26]. Available from: https://www-nds.iaea.org/pgaa/databases.htm.
35. Fujimoto N, Tanaka H, Sakurai Y, Takata T, Kondo N, Narabayashi M, *et al.* (2015) Improvement of depth dose distribution using multiple-field irradiation in boron neutron capture therapy. *Appl Radiat Isot,* ***106:*** *134–138*.

[Downloaded from ijrr.com on 2026-11-29]

[DOI: 10.18869/acadpub.ijrr.16.1.33]

[DOI: 10.18869/acadpub.ijrr.16.1.33] [Downloaded from ijrr.com on 2026-11-29]